Engineering 3-D Li-Ion Electrodes with Enhanced Charge Storage Properties Based on Solution-Processed and Sintered Anatase Nanocrystal-Carbon Mesoporous Structures

Micah J. Sussman,[†] Nicolas Brodusch,[†] Raynald Gauvin,[†] and George P. Demopoulos*,[†]

[†]Materials Engineering, McGill University, 3610 University Street, Montreal, Quebec H3A 0C5, Canada

Ⓢ *Supporting Information*

ABSTRACT: Three-dimensional (3-D) monolithic electrodes are an excellent platform for enhancing the electrochemical properties of Li-ion batteries, but fabrication involves complex, difficult to scale-up processing. Current electrode fabrication based on polymeric binder-based pastes of the active material and carbon is expensive and requires volatile toxic organic solvents. Here, aqueous-synthesized anatase (~6 nm) is used as active material in a green fabrication process employing controlled sintering at 450 °C of an ethanolic paste to engineer mesoporous 3-D structures. This enables construction of self-supporting electrodes endowed with a percolating carbon network with enhanced conductivity that exhibit highly stable cycling performance. As such, the new 3-D electrodes achieve greater capacity (185 vs 145 mAh g^{-1} at 1C rate) than standard PVDF binder-based electrodes, and serve as a new approach toward easily scalable and sustainable electrode manufacturing applicable to various active materials.

KEYWORDS: *Lithium-ion batteries, TiO$_2$, 3-D electrodes, fabrication, energy storage*
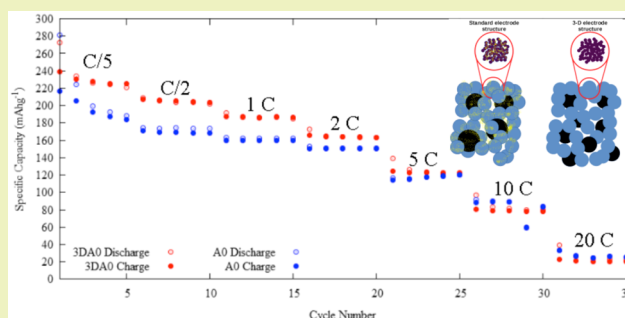
■ INTRODUCTION

Commercially, electrodes for lithium-ion batteries are fabricated using a paste of particulate active insertion material, conductive carbon, and a polymeric binder,[1] usually poly(vinylidene) fluoride (PVDF) in an *n*-methyl 2-pyrrolidone (NMP) solvent. After applying the paste as a thin film on the metallic current collector (Al or Cu), drying typically at 120 °C and pressing, the porous electrode structure is obtained. Avoidance of use of harsh chemicals, such as NMP, has motivated researchers to investigate alternative, environmentally friendly polymer compounds, such as carboxymethyl cellulose, styrene butadiene rubber, and others, which are soluble in water.[2−5] However, these binders still add nonelectroactive mass to the electrode reducing its specific energy. Another problem of the fabrication process is that the resultant particle-carbon-binder composite does not achieve full ionic and electronic conductivity properties of its active and conductive components due to poor percolating interparticle and carbon networking.[6] This has prompted research into alternative fabrication methods not involving particles or binders. Monolithic and other binder-free electrodes that provide a three-dimensional (3-D) electrode structure show promise for use as both anode and cathode,[7−9] but typically they are not prone to large scale manufacturing. This is exemplified with the efforts previously made in fabricating 3-D TiO$_2$ electrodes. Nanostructured TiO$_2$ and, in particular, its anatase polymorph is recognized as excellent substitute for graphite in negative Li-ion electrodes due to its

nontoxicity, safety, and high rate capability.[10] It has also attracted interest in fabricating 3-D electrodes using various techniques like titanium anodization, sputtering, templating, and electrospinning.[11−15] Of these methods, the most notable is electrospinning of TiO$_2$ fibers using an organic precursor solution followed by uniaxial pressing and calcining at 450 °C, as described by Lee et al.[13] This fabrication process resulted in 3-D TiO$_2$ electrodes with higher charge capacity attainment (188 vs 155 mAh g^{-1} after 100 cycles at 0.2C) than conventionally fabricated electrodes, proving that the 3-D electrode concept holds a lot of promise.

All of the proposed 3-D electrode fabrication techniques, however, are both complex and costly to implement (requiring templates[12] or sputtering[15]) or make use of special nanostructures other than nanoparticles and black carbon that the industry favors. For example, the electrospinning technique, which yielded electrodes with the best properties, produces TiO$_2$ nanofibers via a low throughput and expensive organic precursor solution method. Industry, as it positions itself to provide next-generation Li-ion batteries for the emerging electric vehicle transportation sector, has a need for cost-competitive and easily scalable synthesis and fabrication technologies for nanoparticle-based electrodes.[16] In response,
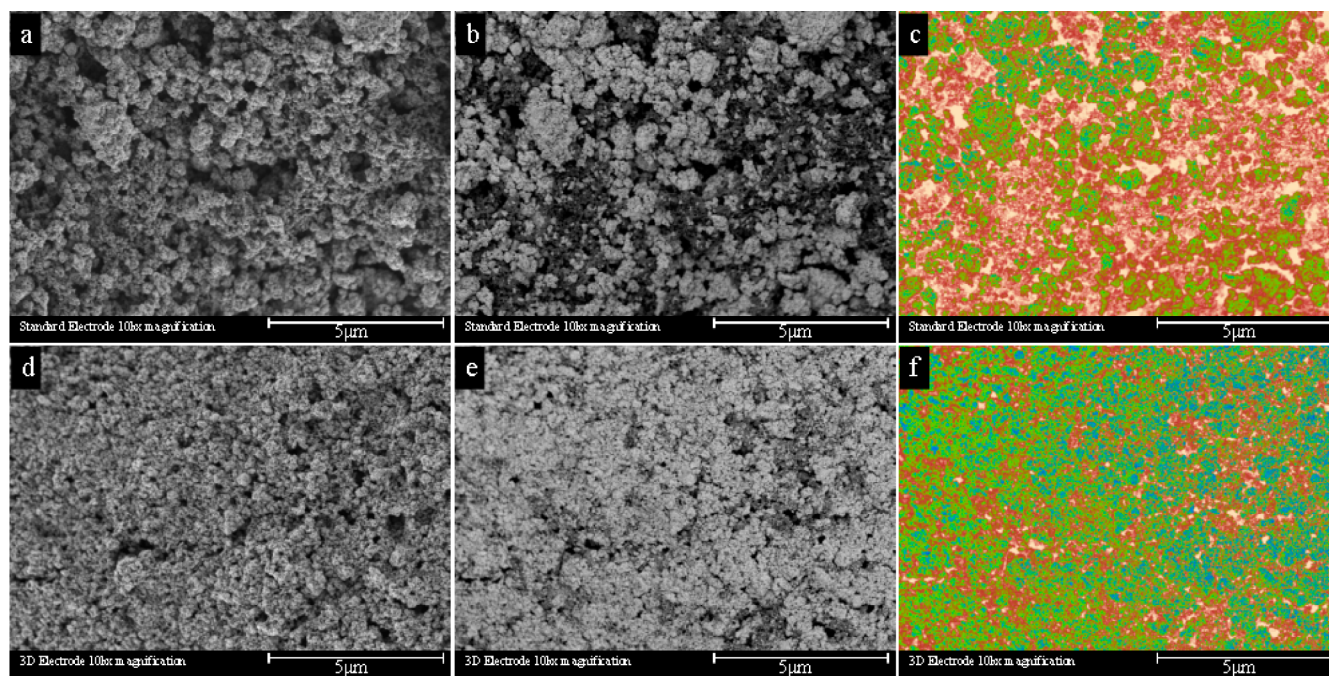
Figure 1. SEM micrographs showing topographical, composition, and compositional "heat maps" for standard (a−c) and 3-D (d−f) electrodes. Heat maps (c and f) reveal electrode macropores (white), carbon (red), TiO_2 (green), and mesopores within TiO_2 aggregates (blue).

we develop fully solution processable 3-D electrode structures using screen printable nanoparticle pastes and sintering.[17] This new template-free 3-D electrode fabrication approach is demonstrated in the case of nanoanatase anodes, but can easily be adapted for other anode or cathode nanoparticle materials. The anatase used as the active material is produced via aqueous solution synthesis in scalable stirred tank reactors in the form of 5−10 nm nanocrystals. This material was recently evaluated in standard electrodes and found to store Li ions via intercalation and pseudocapacitance, the relative contribution of each depending on the thermal treatment history of the anatase nanocrystals.[18] We report in this work that by engineering the novel 3-D sintered electrodes the anatase nanocrystalline particles deliver higher reversible storage capacity than in standard (PVDF binder-based) electrode configuration via induced interparticle necking and optimized percolating carbon networking.[19] The new fabrication method provides a platform for superior nanoparticle-based Li-ion battery electrodes employing easily scalable processing steps.

EXPERIMENTAL SECTION

TiO$_2$ Synthesis. Aqueous synthesized anatase nanoparticles were used as the active material in all electrodes. Their organic-free scalable synthesis was made via forced hydrolysis of an aqueous solution of $TiCl_4$ at 80 °C using a continuous-stirred tank reactor as described in a previous publication.[18] During a test run, 0.1 M $TiCl_4$ is pumped into the reactor and neutralized with NH_4OH or NaOH to pH = 3. After a steady-state residence time of 30 min is attained, the forced hydrolysis process results in a colloidal suspension of anatase nanoparticles, which are centrifuged and washed in deionized water four times and once in anhydrous ethanol before being dried overnight at 80 °C and ground manually to powder form.

Electrode Fabrication. Aqueous synthesized anatase was used as the active material whereas acetylene black (Sigma-Aldrich) was used as a conductive additive in all electrodes. For standard electrodes PVDF (HSV 900, Arkema) was used as the binder, with NMP (Sigma-Aldrich) as the solvent. Aluminum foil was used as the current

collector for all electrodes. Substrates were first pretreated with 1 M NaOH solution to improve adhesion of pastes and prevent delamination.

Standard electrodes were fabricated by mechanically mixing 6 nm anatase nanocrystallites, acetylene black, and a sol of PVDF mixed with excess NMP to produce a paste with a by-weight ratio of 80:10:10 respectively. The paste was deposited by doctor blading on aluminum foil and dried for 24 h at 120 °C. The 3-D electrodes were fabricated using the method we developed and described earlier after making some modifications.[17] The 3-D electrodes had a final composition of 90 wt % anatase and 10 wt % carbon. Anatase and carbon were diluted to a colloidal suspension with anhydrous ethanol, then stirred and sonicated before and after adding α-terpineol and ethyl cellulose (rheological agent and spacer, respectively). The suspension was then evaporated to form a paste with the desired viscosity using a rotary evaporator. The resulting paste was either doctor-bladed or screen-printed onto an aluminum foil substrate, and dried at 80 °C overnight before annealing/sintering at 450 °C following a specific heating profile (see Figure S6 in the Supporting Information).[20] More details on the fabrication of the 3-D electrodes can be found in the Supporting Information.

Physical Characterization. Transmission electron microscopy (TEM, Philips CM200) was used at 200 kV to determine particle morphology and crystal structure. TEM specimens were prepared by depositing particles on a copper grid. Brunauer−Emmett−Teller (BET) surface area analysis was performed using a Micromeritics TriStar 3000 apparatus to determine surface area, particle size, and pore size distribution (BJH method). SEM micrographs were taken using cold-field emission scanning electron microscopy (CFE-SEM, Hitachi SU−8230, Hitachi High Technologies, Rexdale, Canada) providing high brightness and stable current due to the autoflash technology. The working distance was between 1 and 3 mm, and a final landing voltage of 0.5 kV was used. Two through-the-lens detectors were used for secondary (SE) and backscatter (BSE) electron imaging. A filtering grid was used with the top detector in some images to remove SEs and low energy BSEs from the total signal reaching the top detector and was labeled Fx, x being the filtering grid bias value (percentage of the deceleration voltage). X-ray mapping was done using a four segments annular retractable Bruker Flat Quad detector located on top of the specimen. The accelerating voltage was
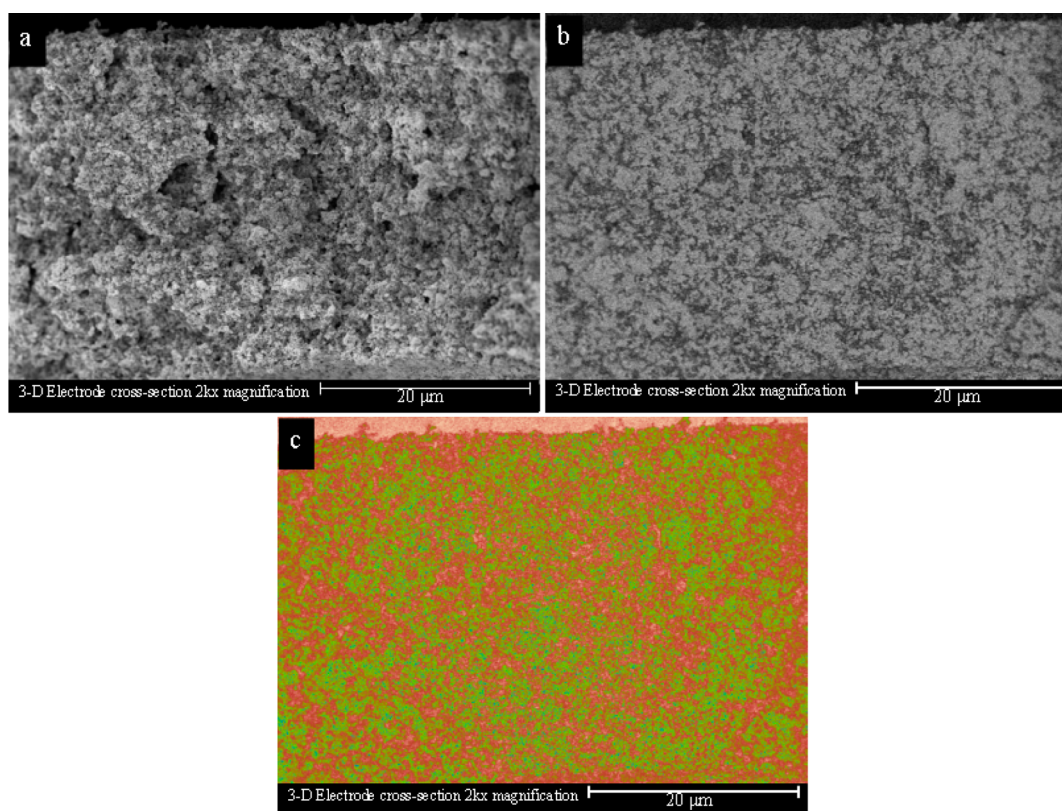
Figure 2. Cross section of 3-D electrode film displaying percolating carbon networks as a topographic micrograph (a), compositional micrograph (b), and a heat map (c) that associates the two images.

2 kV and the working distance 10 mm. Image processing was performed on electron micrographs to reveal nanoscale data on compositional and topographical features within the electrodes. Details of this process are available in the Supporting Information.

Electrochemical Characterization. Electrochemical characterization was performed using Swagelok-type cells tested using a BioLogic VSP potentiostat/galvanostat/EIS system. Half cells were constructed in an argon-filled glovebox using the titania electrodes as the working electrodes and lithium foil as the counter electrode. The electrolyte used was 1 M LiPF$_6$ in EC:DMC:DEC (2:2:1 by weight) mixed solvent (BASF). Galvanostatic charge and discharge was performed between 1 and 3 V for 100 cycles at both 168 and 1680 mA g^{-1}, representing 1C and 10C rates, respectively. Rate capability with equal charge and discharge currents was performed at C/5, C/2, 1C, 2C, 5C, 10C, and 20C rates. For all cells, discharge was performed first to insert lithium into pristine TiO$_2$.

RESULTS AND DISCUSSION

Mesoporous Electrode Structure. The aqueous synthesized anatase nanoparticles used in both the standard and 3-D electrodes were approximately 6 nm in diameter with 222 m^2 g^{-1} surface area. SE and BSE micrographs of both standard and 3-D electrodes elucidate stark differences that affect performance. Figure 1 shows topographic and constitutional information on both type electrode films. Figure 1a−c,d−f is of the same regions in the standard and 3-D electrodes, respectively. In both cases, the nanoparticles aggregate to form mesoporous microparticles. This allows the electrolyte to enter the structure of the electrode and interact with the surface of the particles. However, the first significant difference between the two electrode types is the size of aggregates seen in Figure 1a,d. The 3-D electrode has much smaller aggregates (Figure 1d), which can be attributed to the use of rheological

dispersants (terpineol/ethyl cellulose) and ultrasonication. The TiO$_2$ nanocrystallites aggregate to form larger, mesoporous secondary particles, but in the standard electrodes, as only mechanical mixing is employed, these aggregates are much larger. Investigating the composition in Figure 1b,e, where light colored regions represent TiO$_2$ and dark colored regions represent carbon, the 3-D electrodes have uniform intermixing, as opposed to the significant segregation associated with the standard electrodes. Heat maps of the two type electrodes are shown in Figure 1c,f. The heat maps were built by associating a color gradient to the black-to-white threshold gradient associated with the compositional images (Figure 1b,e). This allows for colors to be associated with various features in the image, making it easier to understand what is seen. White is associated with macroporosity in the electrode, red is associated with carbon, green is associated with TiO$_2$, and blue is associated with mesoporosity in the TiO$_2$ aggregates. Examining the heat maps in Figure 1c,f once more, it becomes evident that the carbon is homogeneously distributed through the TiO$_2$ matrix in the case of the 3-D electrode but not in the standard electrode. However, the micrographs in Figure 1 show only the surface of the electrodes. The excellent microstructure of the 3-D electrode can be further evaluated by examining its cross-section shown in Figure 2. As seen throughout the thickness of the film (~60 μm), carbon and TiO$_2$ nanocrystals are uniformly distributed with carbon, providing a conductive percolating network. Finally, Figure 3 shows a high magnification secondary electron micrograph of the 3-D electrode that clearly reveals sintering to have induced interparticle necking, resulting in a porous monolithic structure that provides physical support and excellent interfacing with the electrolyte for enhanced Li-ion intercalation pathways. It is the
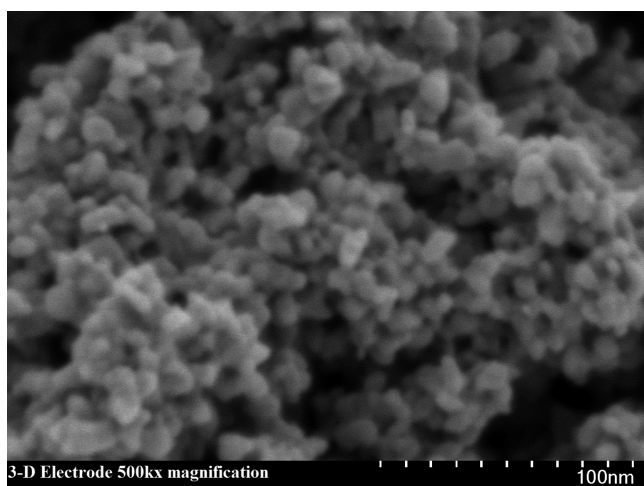
Figure 3. High magnification secondary electron micrograph of the 3-D electrode structure.

interparticle necking that provides the electrode with its 3-D structure. As necking occurs, the nanoparticles bond to form an interconnected rod-like structure. In the standard electrode, however, there is no consistent structure and particles are held together at individual contact points via the polymer binder. The heat map in Figure 1c suggests that the particles are coated by the binder with the latter further filling part of the mesoporous space leading to an adverse effect on electrolyte infiltration and thus Li-ion insertion.

Pore size characterization (data shown in Supporting Information, Figures S2 and S3 and Table S1) of the two electrode types confirmed the superior porous structure of the 3-D electrode configuration. After fabrication, the standard and 3-D electrode films were removed from the current collector so the porosity could be investigated. The shape of the isotherm of each film is the same, and is indicative of mesoporous material. The lower adsorption and desorption as compared to the particulate anatase indicates a lower surface area. During the sintering process (applicable to 3-D electrodes), interparticle necking occurs as well as some particle coarsening associated with the elevated temperature associated with sintering. However, the standard films are not exposed to high temperature; this implies that the observed reduced surface area is not due to crystallite coarsening but rather as already mentioned should be associated with binder coating of particles. To adhere particles together, the binder must partially coat the particles. This is explained by the difference in pore size between the two electrodes. Therefore, it is postulated, on the basis of high resolution SEM imaging and BJH pore size analysis, that the PVDF polymeric binder fills part of the pore space via surface attachment/coating hence the smaller pore size, which has as consequence to interfere with Li-ion shuttling at the particle/electrolyte interface. This is another undesirable side effect of the conventional binder-based electrode fabrication practice, highlighted schematically in Figure S4 (Supporting Information).

Figure S3 (Supporting Information) shows the pore size distribution for the two electrode films. The standard film has an average pore size of 7.6 nm, making it mesoporous, with secondary 25 nm pores forming due to aggregation of nanoparticles. The 3-D electrode has an average pore size of 15 nm, but as the figure shows, there are maxima at 22, 17, and 10 nm. The dispersants added to the paste formulation, as well

as ultrasonication, help to limit the aggregation of nano-crystallites into large secondary particles. Although aggregation does occur, the limited size allows for a hierarchical pore structure to develop. Pore formation is facilitated in the 3-D electrode via volatilization of the organic paste components, namely α-terpineol and ethyl cellulose.

Electrochemical Performance. Figure 4 shows the galvanostatic cycling at 1C (168 mA g^{-1}) over 100 cycles. In
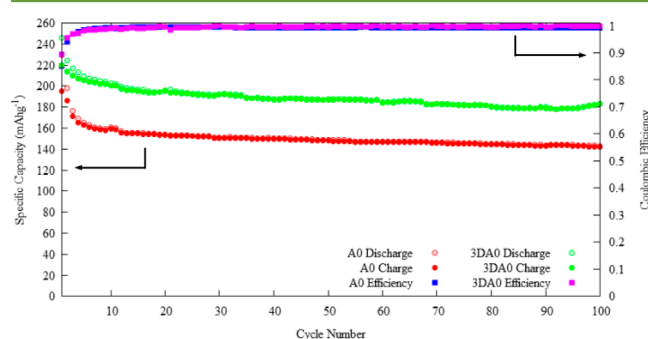

Figure 4. Galvanostatic charge/discharge over 100 cycles between cutoff voltages of 1 V (discharge) and 3 V (charge) at 1C rate (168 mA g^{-1}).
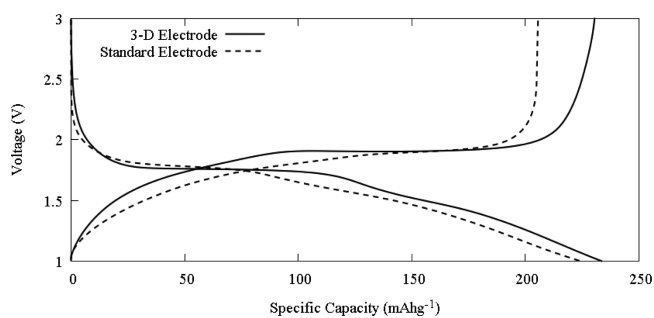

Figure 5. Voltage−capacity profiles for standard (solid line) and 3-D (dashed line) electrodes during the initial lithiation and delithiation cycle at C/5 rate.

the initial cycle (Figure 5), the standard electrode lithiates (discharge) to $x = 0.68$ in Li$_x$TiO$_2$, the equivalent of 229 mAh g^{-1}, and has a charge (delithiation) capacity of 196 mAh g^{-1} ($x = 0.58$). The 3-D electrode, however, achieves 245 mAh g^{-1} during lithiation and 219 mAh g^{-1} during delithiation ($x = 0.73$ and 0.65, respectively). This gives initial efficiencies of ∼85% and 90% for the standard and 3-D electrodes, respectively. As the electrodes cycle (Figure 4), they both achieve nearly 100% Coulombic efficiency over 100 cycles; however, the 3-D electrode has a much higher capacity retention, as the standard electrode loses 30 mAh g^{-1} of reversible capacity during the next 10 cycles, whereas the 3-D electrode loses only 20 mAh g^{-1}. After 100 cycles, the reversible capacity of the standard electrode is approximately 145 mAh g^{-1} while the 3-D electrode retains approximately 185 mAh g^{-1}, a 27% higher capacity retention.

This increase in capacity can be explained by the better ionic and electronic conductivity properties of the 3-D porous electrode structure. Thus, as already described earlier, the improved nanoTiO$_2$/carbon dispersion creates an effective percolating conducting network that results in higher capacity

as also observed by Bresser et al.[19] While in the latter work, TiO_2 was in the form of nanorods synthesized by an expensive colloidal route that does not render easily to scale-up here nanoparticles are used that thanks to interparticle necking that occurs as a result of sintering (Figure 3) build a mesoporous monolith with optimum electrolyte contacting. Although particle interconnectivity boosts performance, the sintering itself plays an additional role in attaining higher capacity. As we have reported elsewhere,[18] increased crystallinity allows for lithium to insert more easily into the octahedral sites of anatase due to favorable diffusion pathway leading to increased capacity. In this case, the sintering step acts as a controlled anneal increasing crystallinity. As such, there is an increase in diffusion-based Li-ion storage, the major insertion mechanism below 4C rate.

As shown in a recent study, the relative contribution of diffusion-based (intercalation) and pseudocapacitive storage depends on the degree of crystallinity and surface area of the anatase.[18] This intrinsic behavior of nanoanatase as Li-ion host material manifests in this work when the rate capability of the 3-D electrodes is examined (Figure 6). At low rates (up to 5C),
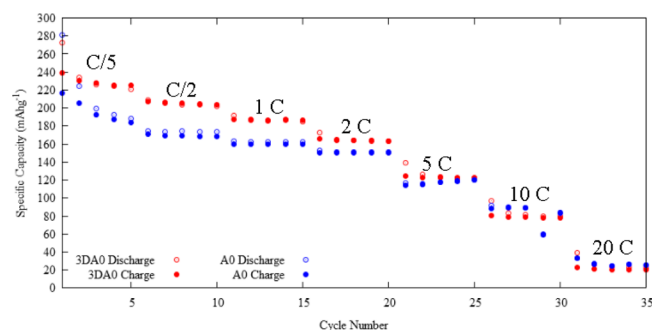

Figure 6. Galvanostatic cycling of standard and 3-D electrodes at various rates between cutoff voltages of 1 and 3 V.

the 3-D electrode exhibits a higher capacity than the standard electrode; thereafter, the two electrodes have nearly the same capacity, e.g., 105/115 mAh g^{-1} for the 3-D/standard electrodes respectively cycled at 10C rate for 100 cycles (Figure S5, Supporting Information). Due to sintering, the 3-D electrode's anatase particles have better crystallinity, a property that favors diffusion-based storage over pseudocapacitance,[18] hence its higher capacity at a low rate (Figure S7, Supporting Information. At the same time, sintering leads to reduction of surface area (from 222 m^2/g of the nonsintered crystallites reduced to 100 m^2/g for the 3-D sintered film) that causes significant loss of pseudocapacitive storage, hence the lower performance at higher rate. With optimized crystallinity and surface area, the 3-D electrode is able to maximize the amount of charge stored. At a low rate, diffusion-based mechanisms control the storage until $Li_{0.5}TiO_2$, whereas pseudocapacitive mechanisms allow storage on the surface of the electrode structure. It is also possible that during sintering the composite C/TiO_2 electrode develops Ti^{3+} and oxygen vacancies in the TiO_2, which can have a positive effect on Li-ion storage in analogy with photocatalytic studies.[21,22] This effect is expected to be rather limited though here as significant Ti^{3+} and oxygen vacancy formation is reported to occur on the surface of TiO_2 principally at temperatures above 400 °C under vacuum or reducing atmosphere.[22]

Effects of Controlled Sintering Profile. It is important that sintering is carefully optimized to obtain minimum loss of surface area while still achieving the 3-D structure via interparticle necking, crystal annealing, and mesopore creation via volatilization of the paste organic components. This is optimally achieved in the present system with the thermal profile described in Figure S6 (Supporting Information). It is due to this sintering profile that the electrochemical properties are enhanced compared to those of the annealed samples in previous work.[18] In this case, the temperature is increased quickly and held for shorter times, which results in increased crystallinity with less surface area loss. In previous work, the surface area decreased 50% before use in the electrode, which as previously mentioned decreases surface area further. In this case, there is a similar loss in surface area; however, the particles are already in the electrode structure as it happens. To demonstrate the importance of sintering temperature/time conditions, we prepared two 3-D sintered electrodes, one following the profile of Figure S6 (Supporting Information) and one following the profile of Figure S7 (Supporting Information) featuring longer heating time at 400 °C. The temperature profile is similar to that of Figure S6 (Supporting Information) until it reaches 325 °C, where it ramps directly to 400 °C. This allows for the burnout/volatilization of α-terpineol/ethyl cellulose, crystal annealing and interparticle necking. The temperature then decreases to 25 °C the same way as the original profile did.

Rate capability electrochemical testing was performed on the two sintered 3-D electrodes with the optimum sintering profile (Figure S6, Supporting Information) and the nonoptimized sintering profile (Figure S7, Supporting Information). The results are shown in Figure S8 (Supporting Information). At the C/5 rate, the formation cycle of the 400 °C annealed sample (3D400) (profile in Figure S6, Supporting Information) has an initial insertion capacity of 296.4 mAh g^{-1}, which is the equivalent of $x = 0.88$ in Li_xTiO_2, almost the theoretical capacity of anatase (335 mAh g^{-1}). This is compared to the standard profile electrode (3D), which is a bit lower at 272.2 mAh g^{-1} ($x = 0.81$ in Li_xTiO_2). However, the charge (delithiation) capacities for 3D400 and 3D are in the reverse order, i.e., 194 and 238 mAh g^{-1}, respectively. That is, the oversintered electrode exhibits large polarization. As the electrodes cycle, even at a low rate, there is sizable capacity loss in 3D400 that is not seen in 3D. The Coulombic efficiencies finally equalize at just under 100%; however, at this point, the capacity difference between the two electrodes is extremely high. This set of electrochemical data proves that sintering needs to be carefully conducted by balancing the requirements for interparticle necking, crystal annealing, and pore creation without excessive particle coarsening and surface area loss.

■ CONCLUSIONS

We have demonstrated a novel electrode fabrication method using 6 nm aqueous synthesized anatase nanocrystals as active Li-ion host material. A controlled sintering procedure provided optimal 3-D structure without losing surface-area-based storage capability. These 3-D sintered electrodes have superior electrochemical properties. Further, the excellent intermixing of active particles and carbon achieved with the novel formulation and controlled sintering step leads to a highly conductive percolating carbon network. It is clear that this 3-D binder-free sintered electrode structure has potential to provide

superior electrodes in a scalable and cost-effective way. Although TiO_2 was used as active material, it serves only as a platform to demonstrate the 3-D electrode engineering concept, which can be adapted for use with other active materials to produce cells with superior properties, meeting the ever-increasing demand for cost-competitive advanced Li-ion batteries by the electric vehicle industry.

■ ASSOCIATED CONTENT

Ⓢ Supporting Information

Physical (transmission electron micrographs, BET surface area, BJH pore size) and electrochemical characterization data and sintering profiles for the electrodes. This material is available free of charge via the Internet at http://pubs.acs.org/.

■ AUTHOR INFORMATION

Corresponding Author

*G. P. Demopoulos. E-mail: george.demopoulos@mcgill.ca. Tel.: (514) 398-2046.

Notes

The authors declare no competing financial interest.

■ ACKNOWLEDGMENTS

■ REFERENCES

(1) Li, J.; Daniel, C.; Wood, D. Materials processing for lithium-ion batteries. *J. Power Sources* **2011**, *196*, 2452−2460.

(2) Li, J.; Lewis, R. B.; Dahn, J. R. Sodium carboxymethyl cellulose: A potential binder for Si negative electrodes for Li-ion batteries. *Electrochem. Solid State Lett.* **2007**, *10*, A17−A20.

(3) Mancini, M.; Nobili, F.; Tossici, R.; Wohlfahrt-Mehrens, M.; Marassi, R. High performance, environmentally friendly and low cost anodes for lithium-ion battery based on TiO_2 anatase and water soluble binder carboxymethyl cellulose. *J. Power Sources* **2011**, *196*, 9655−9671.

(4) Morretti, A.; Kim, G.-T.; Bresser, D.; Renger, K.; Paillard, E.; Marassi, R.; Winter, M.; Passerini, S. Investigation of different binding agents for nanocrystalline anatase TiO_2 anodes and its application in a novel, green lithium-ion battery. *J. Power Sources* **2013**, *221*, 419−426.

(5) Liu, J.; Zhang, Q.; Wu, Z.-Y.; Wu, J.-H.; Li, J.-T.; Huang, L.; Sun, S.-G. A high-performance alginate hydrogel binder for Si/C anode of Li-ion battery. *Chem. Commun.* **2014**, *50*, 6386−6389.

(6) Chen, Y.-H.; Wang, C.-W.; Zhang, X.; Sastry, A. M. Porous cathode optimization for lithium cells: Ionic and electronic conductivity, capacity, and selection of materials. *J. Power Sources* **2010**, *195*, 2851−2862.

(7) Lee, K.-T.; Lytle, J. C.; Ergang, N. S.; Oh, S. M.; Stein, A. Synthesis and rate performance of monolithic macroporous carbon electrodes for lithium-ion secondary batteries. *Adv. Funct. Mater.* **2005**, *15*, 547−556.

(8) Wang, X.; Liu, B.; Xiang, Q.; Wang, Q.; Hou, X.; Chen, D.; Shen, G. Spray-painted binder-free SnSe electrodes for high-performance energy-storage devices. *ChemSusChem* **2014**, *7*, 308−313.

(9) Ha, D.-Y.; Islam, M. A.; Robinson, R. D. Binder-free and carbon-free nanoparticle batteries: A method for nanoparticle electrodes without polymeric binders or carbon black. *Nano Lett.* **2012**, *12*, 5122−5130.

(10) Weng, Z.; Guo, H.; Liu, X.; Wu, S.; Yeung, K. W. K.; Chu, P. K. Nanostructured TiO_2 for energy conversion and storage. *RSC Adv.* **2013**, *3*, 24758−24775.

(11) Ortiz, G. F.; Hanzu, I.; Djenizian, T.; Lavela, P.; Tirado, J. L.; Knauth, P. Alternative Li-ion battery electrode based on self-organized titania nanotubes. *Chem. Mater.* **2009**, *21*, 63−67.

(12) Brezesinski, T.; Wang, J.; Polleux, J.; Dunn, B.; Tolbert, S. H. Templated nanocrystal-based porous TiO_2 films for next-generation electrochemical capacitors. *J. Am. Chem. Soc.* **2009**, *131*, 1802−1809.

(13) Lee, S.; Ha, J.; Choi, J.; Song, T.; Lee, J. W.; Paik, U. 3D cross-linked nanoweb architecture of binder-free TiO_2 electrodes for lithium ion batteries. *ACS Appl. Mater. Interfaces* **2013**, *5*, 11525−11529.

(14) Tammawat, P.; Meethong, N. Synthesis and characterization of stable and binder-free electrodes of TiO_2 nanofibers for Li-ion batteries. *J. Nanomater.* **2013**, *2013*, 1−8.

(15) Cheng, J.; Wang, B.; Xin, H. L.; Kim, C.; Nie, F.; Li, X.; Yang, G.; Huang, H. Conformal coating of TiO_2 nanorods on a 3-D CNT scaffold by using a CNT film as a nanoreactor: A free-standing and binder-free Li-ion anode. *J. Mater. Chem. A* **2014**, *2*, 2701−2707.

(16) Chen, J. A review of nanostructured lithium ion battery materials via low temperature synthesis. *Recent Pat. Nanotechnol.* **2013**, *7*, 2−12.

(17) Sussman, M. J.; Brodusch, N.; Gauvin, R.; Demopoulos, G. P. Binder-free fabrication of nanotitania/carbon lithium-ion intercalation electrodes. *J. Electrochem. Soc.* **2013**, *160*, A3100−A3107.

(18) Sussman, M. J.; Yasin, A.; Demopoulos, G. P. On the complex interplay of crystallinity and surface area effects on Li-ion intercalation and pseudocapacitive storage properties of nanocrystalline anatase. *J. Power Sources* **2014**, *272*, 58−67.

(19) Bresser, D.; Paillard, E.; Binetti, E.; Kreuger, S.; Stricolli, M.; Winter, M.; Passerini, S. Percolating networks of TiO_2 nanorods and carbon for high power lithium insertion electrodes. *J. Power Sources* **2012**, *206*, 301−309.

(20) Lee, K.-E.; Charbonneau, C.; Shan, G.; Demopoulos, G. P.; Gauvin, R. Nanocrystalline TiO_2 thin film electrodes for dye-sensitized solar cell applications. *JOM* **2009**, *61*, 52−58.

(21) Li, Y.; Li, X.; Li, J.; Yin, J. TiO_2-coated active carbon composites with increased photocatalytic activity prepared by a properly controlled sol−gel method. *Mater. Lett.* **2012**, *59*, 2659−2663.

(22) Xiong, L.-B.; Li, J.-L.; Yang, B.; Yu, Y. Ti^{3+} in the surface of titanium dioxide: Generation, properties and photocatalytic application. *J. Nanomater.* **2012**, *2012*, 1−13.